Folding model study of α-p scattering: Systematics of elastic scattering, effective interaction, and inelastic excitation of N^* resonances

H. P. Morsch,[1] W. Spang,[2] and P. Decowski[3]
[1]*Institut für Kernphysik, Forschungszentrum Jülich, D-52425 Jülich, Germany*
[2]*Laboratoire National Saturne, CEN-Saclay, F-91191 Gif-sur-Yvette Cedex, France*
[3]*Physics Department, Smith College, Northampton, Massachusetts 01063-1000, USA*
(Received 10 July 2002; published 4 June 2003)

For a description of elastic and inelastic α-p scattering exciting N^* resonances optical potentials and transition potentials were derived by folding nucleon and nucleus mass densities with a variable range effective interaction. For elastic α-p scattering in forward direction, a reasonable description of essentially all data has been obtained from low energies up to the GeV region. Also, α scattering from ^{4}He and ^{12}C is quite well described with potentials, which indicate that the used folding method is a valid approach for the systems in question. The strong energy dependence of the deduced potentials can be accounted for by a sum of scalar and vector meson-exchange potentials and a soft Pomeron-exchange contribution. The scalar meson-exchange potential falls off rapidly with energy and has a large radius in agreement with theoretical predictions. Consistent with the flavor SU(3) quark model, the vector-meson coupling is rather weak in the central potential, but is strong in the spin-orbit potential, for which a soft Pomeron contribution is negligible. The differences between the deduced α-p and nucleon-nucleon (NN) potentials are understood; further, an excellent description of the energy dependence of the s-wave NN amplitudes is obtained in the folding model framework. Distorted wave Born approximation calculations for inelastic α-p scattering show a t-dependence of the $L=0$ cross section consistent with empirical form factors. Absolute yields for excitation of the resonances $P_{11}(1440)$, $D_{13}(1520)$ and $F_{15}(1680)$ were calculated, using resonance shapes from π-N scattering. A quantitative description of the data at $E_\alpha = 4.2$ GeV is obtained using fluid-dynamical transition densities and strengths exhausting large fractions of scalar energy weighted sum rules. The rather pure scalar (non-spin-isospin-flip) character of these excitations and the observed cross sections are in severe conflict with the constituent quark model. Finally, a prediction is made for p-α scattering at an incident energy of $E_p = 2.2$ GeV, which yields strongly increased cross sections for N^* excitations.

DOI: 10.1103/PhysRevC.67.064001 PACS number(s): 25.55.Ci, 25.10.+s, 13.75.Cs, 14.20.Gk

I. INTRODUCTION

The investigation of the structure of baryons and particularly their excitations has received renewed attention due to improved experimental possibilities at new electron and hadron accelerators. Concerning baryon resonances, an interesting aspect for studies with hadronic probes is the selectivity in particular reactions, e.g., in charge-exchange reactions Δ resonances are seen exclusively, whereas in α-p scattering ''scalar'' N^* resonances can be investigated. Such scalar (isoscalar non-spin-flip) N^* excitations deserve special attention, because their structure is not connected in a simple way to the underlying quark structure of baryons. However, there is a direct but not well-understood connection to the scalar part of the strong interaction, which represents the strongest part of the nucleon-nucleon (NN) force at low energies (described by σ or 2π and ω exchange) but also at high energies (multi-gluon-exchange). Therefore, it is of significant interest to investigate elastic and inelastic α-p scattering at energies up to several GeV (5–10 GeV), paying particular attention to the excitation of N^* resonances.

The study of elastic proton scattering from spin zero target nuclei at intermediate energies has received considerable attention over the past 30 years, both experimentally and theoretically (see, e.g., the review by Ray, Hoffmann, and Coker [1]). Theoretically, in addition to the Glauber model [2,3], elastic p-A scattering has been studied in great detail using multiple-scattering optical potentials in a nonrelativistic approach with relativistic kinematics (see, e.g., the full-folding model discussed in Ref. [4]), but also in a relativistic approach solving the Dirac equation [5]. In both approaches an equally good description of the experimental data has been achieved [1]. Most of these studies have been performed for p scattering from heavier nuclei ($A \geqslant 12$). Elastic p-α scattering has been studied in the nonrelativistic approach, using the conventional optical potential [6] and the Glauber model [3,7], and more systematically in the energy region 0.5–2 GeV in the relativistic approach [8] using Lorentz invariant optical potentials.

Concerning inelastic scattering, theoretical studies at higher energies are rather scarce and are limited to a discussion of low lying states of the target nucleus, see, e.g., Ref. [9], or NN-$N\Delta$ coupling [10]. Experimental and theoretical studies of N^* excitation in α-p scattering are discussed in Refs. [11–13].

For our study of elastic and inelastic scattering we used the double folding method in the nonrelativistic approach (applied successfully to nucleus-nucleus scattering [14,15]). However, different from the conventional approach (in which the interaction between point nucleons is considered), extended nucleon densities are used. This allows to derive inelastic transition densities by dynamically changing the

nucleon density (by deformation or shell transition in a quark model). In this approach the ''effective'' interaction acts between the constituents of the projectile and target nucleons.

By adjusting the strength and range of the effective interaction, forward angle α-p scattering is well described and allows us to study the properties of the optical potential in a large energy region. At low energies the interaction is described by meson exchange, for scalar interaction by 2π exchange or σ exchange (see, e.g., Ref. [16]). At higher energies, the interaction is of short range. In a meson-exchange picture, vector-meson exchange (ω and ρ exchange) is assumed. Differently, quark model calculations (see, e.g., Ref. [17]) predict strong core repulsion due to gluon exchange. At high energies multigluon exchange is very strong in the scalar channel and is considered as source of the phenomenological Pomeron exchange (see Refs. [18,19]). Although this process dominates total nucleon-nucleon scattering only at energies well above 10 GeV, soft Pomeron exchange may already contribute to the scalar potential in the energy region in question.

The purpose of this work is to find a reliable description of elastic and inelastic scattering including their interactions over a wide energy region, which allows us to extract spectroscopic information on the structure of N^* resonances. Details of the optical potentials and the results for elastic scattering are given in Secs. II and III. In Sec. IV an interpretation of the energy dependence of the potentials in terms of different exchange contributions is given. Finally, distorted wave Born approximation (DWBA) results for inelastic α-proton scattering are presented in Sec. V, where form factors and scalar excitation of the N^* resonances $P_{11}(1440)$, $D_{13}(1520)$, and $F_{15}(1680)$ are discussed.

II. OPTICAL MODEL DESCRIPTION OF FORWARD ELASTIC SCATTERING

The nuclear optical potential is the standard tool to analyze nucleon-nucleus scattering in a phenomenological way. The Hamiltonian of the combined proton-nucleus system is replaced by an effective one-body Hamiltonian,

$$h(E)=K+U(E), \tag{1}$$

where K denotes the kinetic energy term of the projectile and $U(E)$ the optical potential.

Theoretical derivations of the optical potential are based on approximation schemes to the multiple-scattering series [1]. In the energy region 100–800 MeV, the so-called full-folding model [1,4] is the most successfull method, where the nucleon-nucleus scattering amplitude is expressed by the free nucleon-nucleon scattering amplitude $t(E)$. The optical potential for elastic scattering can be expressed by

$$U(E,\vec{k}',\vec{k})=\sum_{\alpha=1}^{A}\int\frac{d^3p'}{(2\pi)^3}\int\frac{d^3p}{(2\pi)^3}u_\alpha^\dagger(\vec{p}') \times\langle\vec{k}'\vec{p}'|t(E)|\vec{k}\vec{p}\rangle u_\alpha(\vec{p}), \tag{2}$$

where the sum over α includes all occupied single-particle levels $u_\alpha(\vec{p})$, and $t(E)$ represents the two-body t matrices. Recall the definition of the t matrix,

$$t=v+vgt, \tag{3}$$

where v is the bare nucleon-nucleon interaction and g refers to the two-nucleon propagator.

Given the numerical complexity, the following approximations have been used (see Ref. [1]): (i) neglect of the dependence of the t matrix element on the center-of-mass momentum P, (ii) use of on-shell matrix elements only. Then, expression (2) simplifies to a product in momentum space,

$$U(E,\vec{k}',\vec{k})=\tilde{\rho}_A(\vec{q})\langle\vec{q}|t(E)|\vec{q}\rangle, \tag{4}$$

with $\vec{q}=\vec{k}-\vec{k}'$ and $\tilde{\rho}_A(\vec{q})=(2\pi)^{-3}\Sigma_\alpha\int d^3P u_\alpha^\dagger(\vec{p}')u_\alpha(\vec{p})$.

Love and Franey [20] have expressed the t-matrix elements in momentum space by an expansion in Yukawa terms with different range parameters R_i. For the central part of the optical potential they obtain

$$\langle\vec{q}|t_c(E)|\vec{q}\rangle=4\pi\Sigma_i\frac{v_i^c R_i^3}{1+(qR_i)^2}.$$

In coordinate space this corresponds to $t_c(E,r)=\Sigma_i v_i^c Y(r/R_i)$ with $Y(x)=e^{-x}/x$, giving rise to a coordinate space representation of the optical potential,

$$U(E,\vec{r})=\int\rho_A(\vec{r}_1)t_c(E,\vec{r}-\vec{r}_1)\vec{d}r_1. \tag{5}$$

By introducing an extended nucleon density, the optical potential for α-p scattering corresponds to a double-folding expression,

$$U(E,\vec{r})=\int\int\rho_1(\vec{r}_1)\rho_2(\vec{r}_2)t'(E,\vec{r}+\vec{r}_1-\vec{r}_2)\vec{d}r_1\vec{d}r_2, \tag{6}$$

where $\rho_1(\vec{r}_1)$ and $\rho_2(\vec{r}_2)$ represent ground state densities of target and projectile. The t-matrix element $t'(E,\vec{r}+\vec{r}_1-\vec{r}_2)$ is called effective interaction $u(\tilde{r})$, which acts now between the constituents of target and projectile (in this case between the baryon constituents). For the description of the real and imaginary α-p scattering potential a phenomenological complex effective interaction is used for most of the calculations of Gaussian shape $[u(\tilde{r})=(v_o+iw_o)e^{-\tilde{r}^2/\gamma^2}]$ with v_o, w_o, and range γ fitted to the experimental data. The volume integral of the absolute potential, $I_{|U|}=\sqrt{v_o^2+w_o^2}\int e^{-\tilde{r}^2/\gamma^2}d\tau$, can then be compared with the nucleon-nucleon t matrix, see Secs. III B and IV.

The theoretical investigation of proton-nucleus scattering has confirmed the early expectation [21] that a folding approach should be adequate for incident energies above 100 MeV. Here it should also be mentioned, that a geometrical picture with extended hadron densities as given by the fold-

ing potential (6) appears to be appropriate to describe hadron-nucleon scattering up to high energies well above 20 GeV (see Refs. [19,22]). The aim of the present work is to investigate the features of the effective interaction from low energies up to the GeV region. As will be shown, the folding integral (6) yields results for α-p scattering in good agreement with NN scattering t matrices and NN phase shift amplitudes.

The complete optical potential is given by

$$U_{opt}(E,r)=U_{Coul}(E,r)+U(E,r)+\frac{1}{r}\frac{d}{dr}U_{ls}(E,r)\vec{l}\cdot\vec{s}. \tag{7}$$

The Coulomb potential is used with hard sphere at radius r_c; for the spin-orbit potential the normal Thomas form was used, where the radial part is of Woods-Saxon form (see Sec. II A). For this quite weak potential the uncertainties are too large for a reliable folding description.

The folding integral (6) gives rise to two relations, one which connects the mean square radius of the optical potential, $\langle r_U^2\rangle=(\int r^2U(r)d\tau)/\int U(r)d\tau$, with the sum of the mean square radii of the densities $[\langle r_{\rho_i}^2\rangle=(1/A_i)\int r_i^2\rho_i(r_i)d\tau_i]$ and the effective interaction $[\langle r_u^2\rangle=(1.5/u_o)\gamma^2]$,

$$\langle r_U^2\rangle=\langle r_{\rho_1}^2\rangle+\langle r_{\rho_2}^2\rangle+\langle r_u^2\rangle. \tag{8}$$

This expression is exact for Gaussian forms but is also valid for other shapes of the interaction and the densities. It is also reasonably well fulfilled if one of the densities is of exponential form. The fit to experimental data is only sensitive (apart from the interaction strength) to the mean square radius of the whole potential $\langle r_U^2\rangle$ but not to the radius of the densities or the interaction. The other relation connects the volume integral of the optical potential ($I_U=\int Ud\tau$) to the volume integral of the effective interaction and the target and projectile masses,

$$I_U=A_1A_2I_u. \tag{9}$$

These two relations will be used to test the validity of the double folding method by comparing the extracted radii (8) and the volume integrals of the potentials (9) for different mass systems.

Finally, it should be noted that the structure of our folding potential (e.g., for NN scattering) is more complex than that of meson-exchange potentials that assume an interaction between point nucleons (together with form factors). Relation (9) indicates that the volume integral of our effective interaction (between baryon constituents) should be the same as that of point NN potentials, e.g., that of meson-exchange potentials. However, in our approach finite range effects (which are important for the exchange of more than one pion), e.g., 2π exchange, are included naturally. Even more important, deformations of the nucleon ground state (g.s.) density for $N\rightarrow N^*$ transitions can be taken into account correctly (see Sec. V).

A. Calculations for elastic α-proton and α-nucleus scattering

p-α scattering. Data on differential cross sections and analyzing powers of p-α scattering exist at different beam energies (Refs. [6,7,23–33]), which allow a systematic study of the energy dependence. In most of our calculations (see also Sec. II B) we used a proton density of exponential form with a mean square radius consistent with $\langle r_p^2\rangle=0.67\pm0.02$ fm^2 deduced at high energy [22] and Gaussian densities for the α particle and ^{12}C with $\langle r_\alpha^2\rangle=1.97$ fm^2 [12] and $\langle r_{^{12}C}^2\rangle=5.4$ fm^2 [34]. The range of the effective interaction γ was varied between 1.7 fm at low energy and very small values needed at high energies.

Using for the spin-orbit potential $U_{ls}(r)=V_{ls}(r)+iW_{ls}(r)$ volume Woods-Saxon forms, forward angle scattering is reasonably well described (see Ref. [12]). However, the overall description of the angular distributions is not so good as in the relativistic description [8]. This can be improved by using a more complex spin-orbit potential using volume and surface potentials in the form $V_{ls}^v(r)+(d/dr)V_{ls}^s(r)$ and $W_{ls}^v(r)+(d/dr)W_{ls}^s(r)$. To avoid parameter ambiguities, a smooth energy variation of the parameters has been secured. Resulting fits of differential cross sections and analyzing powers together with the data of Refs. [25,27–29,31] are given in Fig. 1, the parameters are given in Table I. For the spin-orbit potential Woods-Saxon parameters $r_o=0.64$ fm and $a=0.18$–0.25 fm were used. A comparison with the simple fits shows, that the extracted strengths of the central potential are not much different, if a simple volume or a more complicated volume-plus-surface form of the spin-orbit potential was used. The resulting fits are comparable to the Glauber model calculations [3,7] and the relativistic description [8].

At low energies, the differential cross sections are dominated by Coulomb-nuclear interference in the small-angle region, the quality of the fits is about the same as that of ^{3}He-p scattering (Ref. [35]). At larger angles, where exchange contributions are important, our approach is not able to describe the data. With increasing energies these exchange contributions are pushed to larger momentum transfers, and above 250 MeV both differential cross sections and analyzing powers are reasonably well described in a rather large range of t values.

α-A scattering. The scattering of α particles from spin-zero target nuclei can be used to study the central potential without spin-orbit effects. Unfortunately, for such systems much less experimental data are available. For α-α scattering, there are data at $E_\alpha=1.98$, 2.57, and 4.2 GeV (Refs. [32,36]). The forward angle data are well described in the present approach (see Fig. 2), from which a mean square radius $\langle r_F^2\rangle_{\alpha\text{-}\alpha}$ of 3.93 ± 0.10 fm^2 was extracted [12]. These fits are also comparable with calculations using the Glauber model [37]. Further, there are data at $E_\alpha=650$ and 850 MeV [38], however, they do not cover the forward angle region important for our description. In low-energy α-α scattering, the interference between projectile and target recoil α particles is large, and a detailed study is found in Ref. [39] with results consistent with our systematics. Further, the forward angle data in the energy range $E_\alpha=100$–160 MeV [40] are

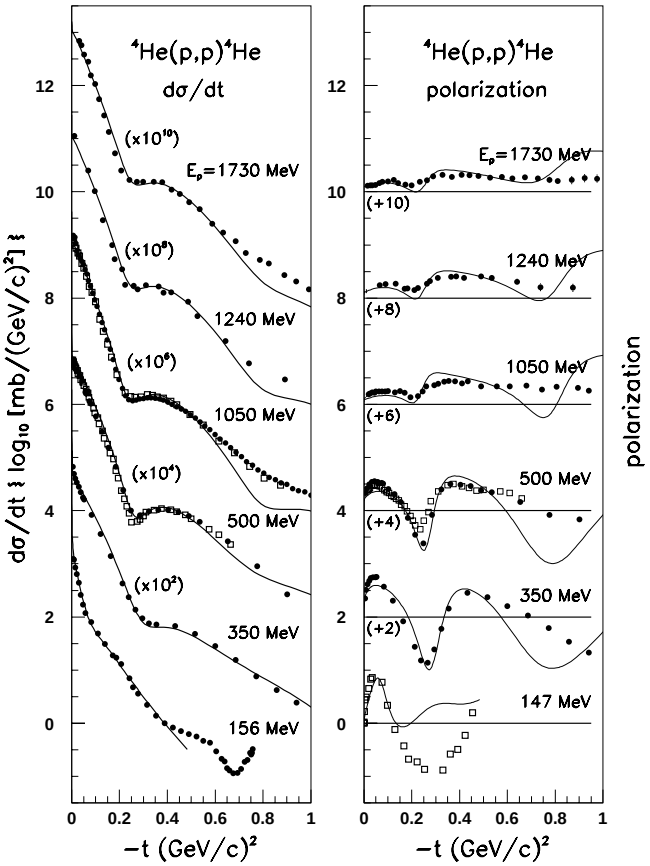

FIG. 1. Calculated differential cross sections and polarization (or analyzing power) for elastic p-α scattering in comparison with the data of Refs. [25,27–29,31]. The cross sections are multiplied by the factors given in brackets; to the polarization the numbers in brackets are added.

consistent with those of p-α scattering. Finally, there are more recent data [41] at $E_\alpha = 280$ and 620 MeV, which are included in our analysis. In this energy region the cross sections fall off by two to three orders of magnitude due to a rapid decrease of the effective interaction. This falloff is satisfactorily reproduced by our calculations.

For α-^{12}C scattering, data exist for $E_\alpha = 1.37$ GeV (Ref. [42]) and 4.2 GeV (Ref. [34]), which are compared in Fig. 2 with our fits, using a mean square radius of 8.2 ± 0.3 fm^2 and 7.4 ± 0.2 fm^2 for the lower and higher energy, respectively. Together with the lower-energy data, two different folding model calculations have been presented [42]; our fits are of similar quality. The parameters are given in Table II, which also includes the results for α-d scattering [34].

B. Test of the consistency of our method

It is important to check whether the potential moments are reliably extracted or still show artifacts due to the choice of the used geometry. For such a check we have used different nucleon densities of Gaussian and exponential form, as well as a Gaussian and Yukawa interaction. It was found that the forward angle cross sections depend only on the strength and radius on the potential (as discussed above) and are not sensitive to the choice of the radial dependence. In particular, the need for smaller range parameters at higher energies is well established.

III. RESULTS FOR THE CENTRAL POTENTIAL

The strengths of the real and imaginary potentials and the mean square radius are quite well determined by our analysis. Beyond this, the behavior of the differential cross sections at small momentum transfers is not very sensitive to the detailed form of the potentials.

A. Mean square radius of the folding potential

In the low-energy region a large range of the effective force is needed in agreement with previous folding model studies (see, e.g., Refs. [15,39,43]). We observe a strong decrease of the range parameter γ up to an incident energy of about 500 MeV. The resulting energy dependence of the mean square radius of the α-p potential $\langle r_V^2 \rangle$ is given in Fig. 3, in which the value extracted at 1.728 GeV is given by the solid line. Using relation (8) equivalent radii can be deduced from α-A scattering, which are given in Fig. 3 by the stars and open circles. An excellent agreement with α-p is obtained when the radii are plotted as a function of the incident energy per nucleon. The error bars represent the estimated uncertainties in the radius determination for different range parameters γ. At small energies the ambiguities between the depth and radius of the potential are eliminated to a large extent by the inclusion of polarization data.

B. Depth of the folding potential

The potentials in Tables I and II show a strong energy dependence. To compare the strengths of the different systems p-α and α-A with NN potentials, our results are given as a function of the equivalent nucleon incident energy E_N^{eq}. This takes into account the fact that in p-α scattering the recoil energy of the scattered nucleon bound in the α particle is reduced due to the higher mass of the α particle, giving rise to a higher center-of-mass (c.m.) energy.

Part of this excess energy E^+ increases the effective energy of the nucleon-nucleon collision and should be added to the beam energy to obtain an equivalent nucleon incident energy E_N^{eq}. In the c.m. frame the equivalent energy $E_{\rm c.m.}^{eq}$ is given by

$$E_{\rm c.m.}^{eq} = E_{\rm c.m.}^{NN} + \mu E_{\rm c.m.}^{+}, \tag{10}$$

where $E_{\rm c.m.}^{+} = [E_{\rm c.m.}^{p\alpha} - E_{\rm c.m.}^{NN}]$ for p-α and $E_{\rm c.m.}^{+} = [E_{\rm c.m.}^{p\text{-}\alpha} + E_{\rm c.m.}^{p\text{-}A} - E_{\rm c.m.}^{NN}]$ for α scattering from complex nuclei. A quite reasonable description is obtained using $\mu \sim 0.2$–0.3.

This effect can be calculated (without free parameter) in the single-particle model, where the nuclear attraction gives rise to an effective increase of the incident energy, related directly to the strength of the complex optical potential $U = V + iW$. For p-α scattering the equivalent energy $E_{\rm c.m.}^{eq}$ can be obtained by replacing the nucleon momentum square p_N^2 by an equivalent value

TABLE I. Summary of the results for p-α scattering. I_v(real) and I_w(imag) represent volume integrals of the real and imaginary potentials, the uncertainties were estimated to be about ± 40 MeV fm^3. For the volume spin-orbit strengths the errors are of the order of 1.5–2 MeV, those for the surface part are significantly larger. The results with asterisk indicate fits of differential cross sections using a volume spin-orbit potential only, for which the parameters are not well determined.

E_p (GeV)	γ (fm)	I_v(real) (MeV fm^3)	I_w(imag) (MeV fm^3)	V_{ls}^v (MeV)	W_{ls}^v (MeV)	V_{ls}^s (MeV)	W_{ls}^s (MeV)
0.031	1.70	−410	60	*			
0.055	1.70	−344	70	*			
0.085	1.68	−215	80	*			
		−246	66	−7.0	5.0	−2.0	3.0
0.156	1.60	−147	90	*			
		−143	80	−2.7	5.5	−6.0	5.0
0.200	1.45	−96	100	*			
		−97	90	−0.3	6.0	−8.0	6.0
0.350	0.62	68	160	*			
		41	132	5.5	7.5	−10.	5.0
0.500	0.35	144	216	*			
		104	224	6.8	8.0	−6.0	5.0
0.648	0.29	190	310	*			
0.800	0.28	196	324	7.5	7.5	−4.0	4.0
1.050	0.26	239	392	*			
		243	384	6.4	7.0	−1.0	3.0
1.066	0.26	217	451	*			
1.240	0.25	287	410	6.0	5.9	1.0	3.0
1.728	0.25	345	562	*			
		325	493	4.5	4.8	2.2	1.5

$$(p_N^{eq})^2 = p_N^2 + 2m_N \overline{U}_\alpha . \tag{11}$$

The potential strength $\overline{U}_\alpha$ is obtained from the volume integral of the total p-α potential ($I_u = \sqrt{I_v^2 + I_w^2}$) in Table I and the mean square radius of the corresponding NN potential. For α-A scattering $\overline{U}_\alpha$ should be replaced by $(\overline{U}_\alpha + \overline{U}_A)$. In Fig. 4 the potential strengths from Tables I and II are shown as a function of the equivalent nucleon energy using Eq. (11). The error bars indicate the uncertainties of the potentials given in Tables I and II.

For the real potential, a good agreement between the results from different systems is found, indicating that relation (9) is also well fulfilled in the whole energy region. The total potential is larger for α-A systems than for p-α. As breakup processes contribute significantly to the imaginary potential, the total potential may be obtained by adding to the imaginary potential $W_{p\text{-}\alpha}$ another absorptive part $W_{p\text{-}A}$ from p-A scattering, which gives

$$U = V + i(W_{p\text{-}\alpha} + W_{p\text{-}A}). \tag{12}$$

Using in first approximation, $W_{p\text{-}A} \sim n W_{p\text{-}\alpha}$ ($n = 1.5$–1.6) yields already a reasonable account of the observed effect. This is shown by the dashed and dot-dashed lines in the lower part of Fig. 4.

In previous work (see, e.g., Ref. [8]) it was found that the strength of the real potential is proportional to $\ln(E_N)$. This

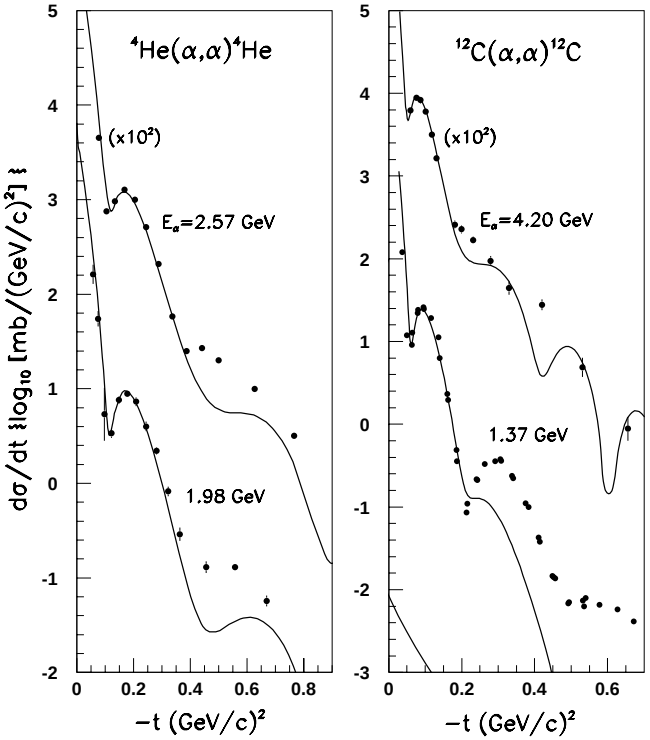

FIG. 2. Calculated differential cross sections for elastic α-A scattering in comparison with the data of Refs. [34,36,42]. The cross sections are multiplied by the factors in brackets.

TABLE II. Summary of the results for α-A scattering, with symbols as in Table I. The uncertainties in the potential depths are almost the same as for p-α scattering.

System	$\frac{1}{4}E_{inc}$ (GeV)	γ (fm)	I_v(real) (MeV fm^3)	I_w(imag) (MeV fm^3)
α-d	1.050	0.3	283	740
α-α	0.070	1.7	−302	114
	0.155	1.6	−62	102
	0.495	0.3	182	442
	0.643	0.3	274	466
	1.050	0.3	350	620
α-^{12}C	0.343	0.7	165	306
	1.050	0.3	439	750

dependence is shown by the dashed line in the upper part of Fig. 4, which is also in good agreement with our results.

The deduced potential strengths may be compared to the strength of the central spin and isospin-independent nucleon-nucleon potential, which is known to exhibit a strong energy dependence (see Ref. [20]). NN t-matrix strengths from Love and Franey [20,44] (at momentum transfer $q=0$) are given in the lower part of Fig. 4 by the solid line. These t-matrix potentials were adjusted to describe the NN phase shifts [45].

We see that the energy dependence of the central NN potential is not very different from our potentials, however,

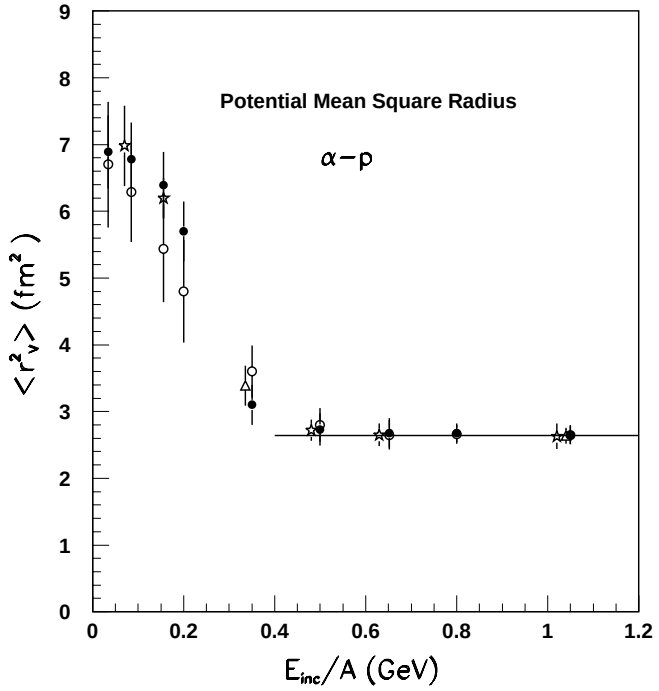

FIG. 3. Mean square radius of the total folding potential for α-p scattering as a function of the incident energy. The open and closed points correspond to p-α scattering (open points represent fits using the usual spin-orbit potential, closed points represent improved fits of cross sections and analyzing powers). The open stars and triangles are deduced from α-α and α-^{12}C scattering, respectively, using relation (8).

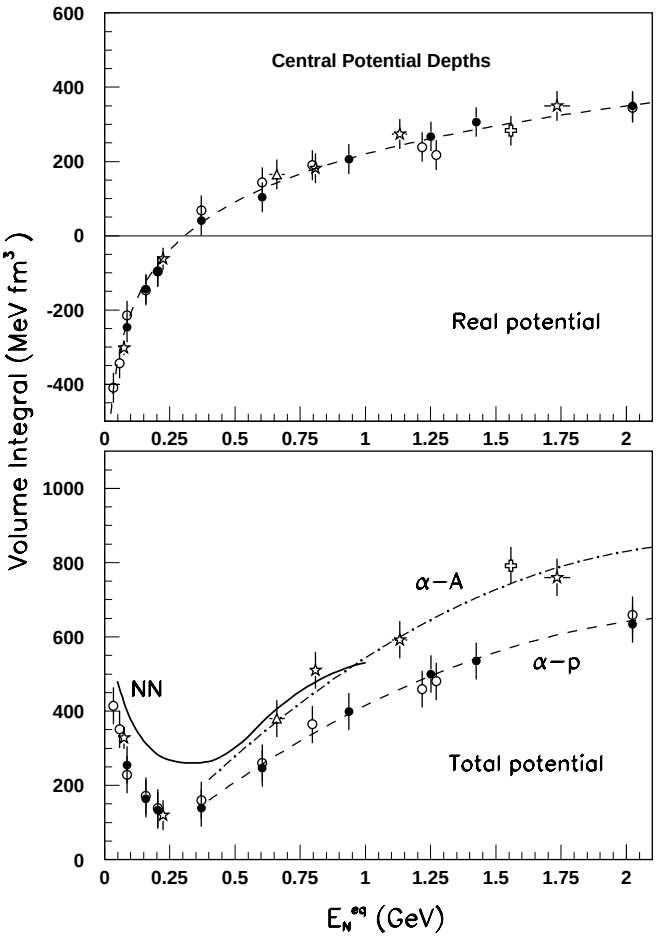

FIG. 4. Depth of the real and total folding potential V and U as a function of the equivalent nucleon incident energy using relation (9) for complex targets. The symbols are the same as in Fig. 3, and the open crosses correspond to α-d scattering. The solid line in the lower part shows the t-matrix strengths from NN scattering [20]. The dashed line in the upper part corresponds to a straight line (as in Ref. [8]), if the potential depths are plotted versus $\ln(E_N)$. The dashed and dot-dashed lines in the lower part show a quadratic fit of the total potential above 400 MeV for α-p and α-A, respectively, using relation (12) for α-A.

the strength of the potential extracted from α-p is generally smaller. At low energies a reduction of the free NN t-matrix strength in the scattering from nuclear systems is known to be due to Pauli blocking, binding energy, and medium corrections. A further reduction of $\leqslant 20\%$ results from contributions of higher momentum transfer ($q>0$) between the colliding nucleons. Taking these effects into account, the differences between the potentials from α-p and NN can be understood qualitatively at low energies [46], see also the results discussed in Sec. IV. However, the differences at the higher energies cannot be explained by nuclear effects.

In Sec. IV we make an attempt to deduce information on the character of the effective interaction from the energy dependence of the potentials. This should also allow to understand the differences found between the α-p and NN potentials. Further, a smooth energy dependence as obtained in this description is advantageous for the DWBA calculations

of inelastic N^* excitations discussed in Sec. V, for which optical potentials at many energies are needed.

IV. HOW CAN WE UNDERSTAND THE ENERGY DEPENDENCE OF THE EFFECTIVE INTERACTION?

The interaction involved in α-p scattering is very selective and contains only contributions from spin- and isospin-independent parts of the nucleon-nucleon force in the central potential. In the following, we describe the energy dependence of the potentials in the whole energy range from low energies up to the multi-GeV region using rather simple parametrizations of possible exchange contributions. These should give a consistent account of both the potential depths and radii.

Concerning meson exchange, only σ (or 2π) and ω exchange can contribute to the real part of the potential, giving rise to an attractive scalar and a repulsive vector potential. For the absorptive potential, ρ exchange may also contribute. The energy dependence of these potentials arises from relativistic effects that are different for scalar and vector potentials. We assume that the linear momentum dependence of the effective potential $V(p)$ is described by the same form as the nucleon-nucleon potentials in Refs. [16,47]. However, in order to fit the strong energy dependence of our potentials, additional ''decay'' form factors $f_{s,v}(p)$ have to be introduced. This yields

$$V^s(p) = -\overline{g_s^2}/m_s^2(1-p^2/2m_N^2) f_s(p) \tag{13}$$

and

$$V^v(p) = \overline{g_v^2}/m_v^2(1+3p^2/2m_N^2) f_v(p). \tag{14}$$

The form factors were used in the form $f_{s,v}(p) = \exp[-\kappa_{s,v}(p-p_0)^2]$ for $p > p_0$ and 1 for $p \leqslant p_0$ with $p_0 \approx c\kappa^{-1/2}$ ($c = 0.15$ for the scalar and 0.45 for the vector potentials). The effective coupling constants $\overline{g_s^2}$ and $\overline{g_v^2}$ were fitted to the data together with the form factor constants κ_s and κ_v.

The strong falloff of the attractive potential (see Fig. 4) at low energies (described by σ exchange) requires a rather steep decrease of $f_\sigma(p)$ with a slope parameter $\kappa_\sigma \sim 3.4\ (\mathrm{GeV}/c)^{-2}$. Fourier transformation of this form factor yields a mean square radius $\langle r_\sigma^2 \rangle \sim 0.80\ \mathrm{fm}^2$, which is quite close to $2\langle r_\pi^2 \rangle \sim 0.84\ \mathrm{fm}^2$. This suggests, that the form factor arises from the ''decay'' $\sigma \rightarrow 2\pi$. For NN scattering c $= 0.45$ (as for the vector potentials), and a smaller slope parameter $\kappa_\sigma \sim 2.4\ (\mathrm{GeV}/c)^{-2}$ is required, which gives $\langle r_\sigma^2 \rangle \sim 0.56\ \mathrm{fm}^2$. Interestingly, the difference in the slope parameters for NN and α-p (which makes the scalar α-p potential more extended) takes into account implicitly a large part of the nuclear effects mentioned in Sec. III B. It should be noted that the introduction of decay form factors for scalar and vector meson exchange (which corresponds to exchange of more than one meson) appears as a quite natural extension of the one-meson exchange picture: at increasing linear momentum p, the relative momenta of the exchanged two or more pions become larger and lead to a falloff of the exchange probability. Expressed by a form factor, the decay constant $\kappa_{s,v}$ is directly related to the width of the scalar or vector meson resonance.

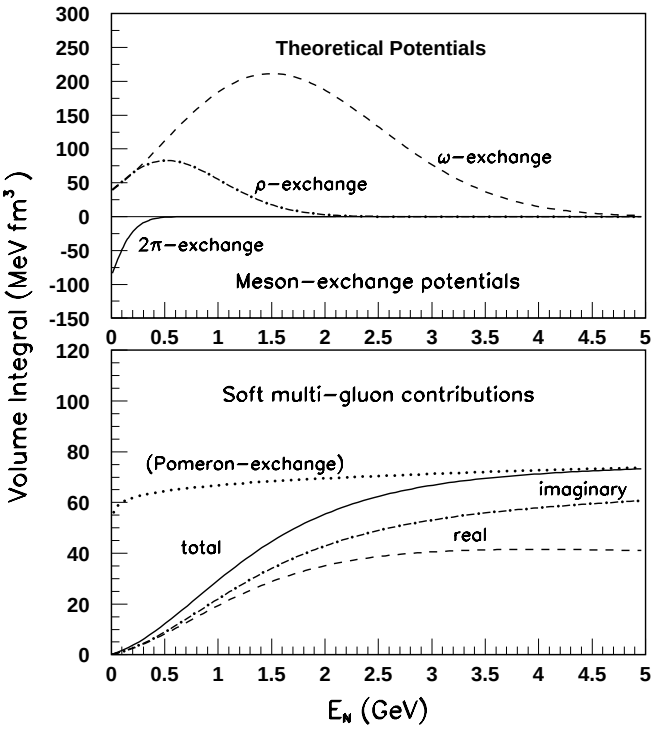

FIG. 5. Energy dependence of the different theoretical potentials discussed in Sec. IV with a coupling strength of 3. The dotted line in the lower part is obtained using $U^P \sim p^{0.08}$.

The form factors for the vector potentials (due to the decays $\omega \rightarrow 3\pi$ and $\rho \rightarrow 2\pi$) have to be used, which are much harder. The decay constant κ_ω is expected to be very small due to the small ω width. To obtain the potentials that extend high enough in energy (more than 3–4 GeV in agreement with experimental information), $\kappa_\omega = 0.3\ (\mathrm{GeV}/c)^{-2}$ was used. The width of the ρ meson is much larger, therefore κ_ρ has to be larger. Its value may be estimated from the contribution to the radius (the details are given in Sec. IV B), which yields $\kappa_\rho \sim 1.0\ (\mathrm{GeV}/c)^{-2}$. With these parameters, the resulting potentials are given in Fig. 5.

A decrease at high energies as obtained for the vector meson-exchange potentials in Fig. 5 is not seen in the experimentally deduced potentials (Fig. 4). The further increase of the optical potentials towards high energies may be accounted for by a multigluon-exchange contribution. At multi-GeV energies, this effect is large and can be described in the Pomeron-exchange picture [18,19], for which well above 10 GeV the energy dependence of the total cross section [18] is given by $\sigma_{tot}(E) \sim s^{0.08}$. This functional form gives rise to a very flat falloff to lower energies. However, at several hundred MeV the strength is far too large in comparison with pp cross sections. Therefore, in this energy domain multigluon exchange has to become small and the interaction is taken over by meson exchange, which is dominant at the lower energies. Microscopically, this effect may be understood by the influence of more complex soft multigluon-exchange dia-

grams (for the scalar channel this contribution may be called ''soft Pomeron exchange''). Phenomenologically, this may be taken into account by a threshold reduction function thr(p) and we write the total soft Pomeron potential in the form

$$U^{sP}(p)=\overline{g^2_{(sP)_t}}/m_c^2\,\mathrm{thr}(p)\left(\frac{p}{p_0}\right)^{0.08}, \qquad (15)$$

with $p_0=1$ GeV/c. For an appropriate description of the data, a very smooth p dependence of thr(p) is needed, for which we used

$$\mathrm{thr}(p)=\left(\frac{\exp(cp)-(1-\epsilon)}{\exp(cp)+1}\right)^4.$$

With values of $c=1.3$ (GeV/c)$^{-1}$ and $\epsilon=0.4$, the results are shown in the lower part of Fig. 5. As soft multi-gluon and meson-exchange contributions can interfere in a microscopic description, c was chosen such that the deviation from the flat Pomeron-exchange potential ends at the energy at which meson exchange has fallen off.

Further, Pomeron exchange at high energies contributes predominantly to the absorptive potential. Differently, for the description of our data in the low energy region, we need contributions to the real and imaginary potential. This appears quite physical, if soft Pomeron exchange develops a rapid energy dependence. To obtain a description of the data consistent with the behavior of total and elastic p-N cross sections, we use the real potential of the form

$$V^{sP}(p)=\overline{g^2_{(sP)_r}}/m_c^2\,\mathrm{thr}(p)\left(\frac{p}{p_0}\right)^{0.08} f_{sP}(p), \qquad (16)$$

and the imaginary potential is then given by $W^{sP}(p)=\sqrt{U^{sP}(p)^2-V^{sP}(p)^2}$. We used $f_{sP}(p)=\exp(-\kappa_{sP}p)$ with $\kappa_{sP}=0.04$ (GeV/c)$^{-1}$, which was adjusted to give the ratio of elastic/total p-p cross sections up to about 10 GeV. The resulting potentials are also given in Fig. 5. For the mass term we used $m_c=600$ MeV, which is much smaller than m_c deduced at high energy [18]. This is justified because at our energies the potential is still sensitive to the whole baryon density (the radial extent is approximately given by $\langle r_\rho^2\rangle \sim 6[(\hbar c)^2/m_c^2]$), whereas at high energies a much smaller part of the baryon density is probed.

A. Depth of the central p-α potential

Calculated potentials are compared in Fig. 6 with the deduced folding potentials. Using for the attractive scalar potential an effective mass m_σ of 520–550 MeV (consistent with [16,47]), a coupling constant $\overline{g_\sigma^2}$ of about 17 is extracted. Due to the form factor cutoff $f_s(p)$, the scalar part falls off quite rapidly with energy, yielding an average coupling strength below 300 MeV, in reasonable agreement with the scalar coupling in the Bonn potential [16,47].

At higher energies vector meson as well as soft Pomeron exchange contribute. A fit of the real potential assuming scalar and vector meson exchange only with a coupling strength

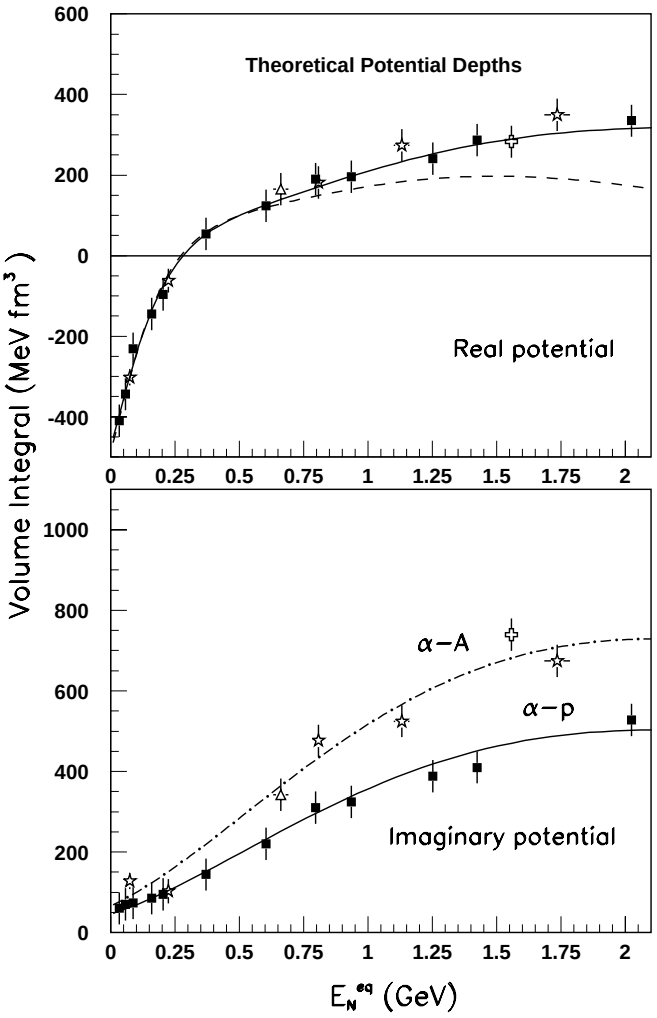

FIG. 6. Calculated depth of the central potential with coupling strengths in Table III in comparison with the data in Fig. 4. The closed squares are average values from α-p, the open symbols are from α-A. The dashed line in the upper part shows a calculation assuming meson exchange only. In the lower part the dot-dashed line is obtained using relation (12).

$\overline{g_\omega^2}$ of 2.8 is shown by the dashed line in Fig. 6. In this way the data in the higher energy region are not described. A fit using all three contributions with strength parameters in Table III is shown by the solid line. In this fit the ω coupling is quite small, as expected from quark model calculations [17].

For the imaginary potential we assume only contributions from the repulsive potentials. This is consistent with the picture that the dominant absorptive process, breakup of the α particle, is caused by short range repulsion. With the parameters in Table III a good description is obtained, see the solid line in the lower part of Fig. 6. Using in addition relation (12), also a quite reasonable description of α-A scattering is obtained (dot-dashed line).

For NN scattering the energy dependence of the central t-matrix potential from Ref. [20] (solid line in Fig. 4) is also quite well described in our approach with couplings given in Table III. In the comparison of p-α and NN potentials in

TABLE III. Deduced coupling strengths for meson and soft Pomeron exchange.

Potential	Coupling			
	$\overline{g^2_{2\pi}}$	$\overline{g^2_{\omega}}$	$\overline{g^2_{\rho}}$	$\overline{g^2_{sP}}$
Central				
p-α real	17	1.5		12
p-α imag		2.7	(0.8)	18
p-α total	17	3.0	(0.8)	22
NN potential [20]	14	6.0	0.8	22
NN s-wave amplitudes[a]	11	$\sim$8	1.1	22
p-α spin-orbit				
Volume real	1.5	0.17	0.32	
Volume imag		0.16	(0.50)	

[a]For the fit in Fig. 9 values of $\overline{g^2_{\pi}}$ of 4.5 and 2.2 and $\overline{g^2_{\omega}}$ of 8.9 and 7.5 were used for the isocalar and isovector case, respectively.

Sec. III B, a discrepancy was found in the higher energy region. This is reflected in the deduced coupling strengths in Table III: the scalar meson and the total soft Pomeron couplings are not very different for p-α and NN, but the ω coupling is much stronger for the NN potential. This can be explained by the spin$=1$ character of the vector potential. In p-α scattering, only the spin projection $\Delta J=0$ contributes, whereas $\Delta J=0$ and 1 amplitudes are present in NN scattering.

Another interesting aspect is the ω coupling constant itself for NN, which was found much stronger in the Bonn potential ($g^2_{\omega}\sim 20$, see Refs. [16,47]) than predicted in the flavor SU(3) quark model (see also the discussion in Ref. [48]). For α-p scattering as well as the central NN potential [20], much smaller values of $\overline{g^2_{\omega}}$ are needed, which are consistent with the flavor SU(3) prediction. To describe NN phase shift amplitudes (discussed in Sec. IV D) somewhat larger ω couplings were required, which may be due to spin-dependent interactions.

B. Mean square radius of the p-α potential

Using the q dependence from Refs. [16,47], the mean square radii of the meson-exchange potentials are directly related to the mass of the exchanged meson by

$$\langle r^2_{V^{s,v}}\rangle = 2\frac{6(\hbar c)^2}{m^2_{s,v}}. \tag{17}$$

To compare these radii with the potential radii, intrinsic core radii arising from additional vertex form factors should be added as well as the contributions from the decay form factors $f_{s,v}(p)$. Concerning the latter, the slope parameter of the scalar form factors yields a contribution $\langle r^2_{f_s}\rangle$ of 0.77 fm^2 for p-α and 0.47 fm^2 for NN. As discussed above, for ω exchange a small slope parameter κ_{ω} is needed, which gives a negligible contribution to the radius. For ρ exchange an estimate of $\langle r^2_{f_v}\rangle$ can be obtained from the difference between isovector and isoscalar radius of the nucleon, $\langle r^2_{f_\rho}\rangle = (\langle r^2_p\rangle_{iv} - \langle r^2_p\rangle_{is})$. The radii $\langle r^2_p\rangle_{iv}$ and $\langle r^2_p\rangle_{is}$ can be obtained from the charge mean square radii of proton and neutron, $\langle r^2_p\rangle_{ch} = 0.74$ fm^2 and $\langle r^2_n\rangle_{ch} = 0.12$ fm^2 [49]. Assuming that the core contributions for ω and ρ exchange are the same, yields $\langle r^2_{f_\rho}\rangle \sim 0.24$ fm^2. This corresponds to a slope parameter $\kappa_\rho \sim 1.0$ (GeV/c)$^{-2}$ used in our calculations.

If we interpret the electromagnetic radii of proton and α particle [50] by vector meson exchange, we need an additional core mean square radius of about 0.25 fm^2. The scalar radius of the nucleon has been found to be much larger [51,52], of the order of 1.5 fm^2. In our description a larger scalar mean square radius is obtained automatically due to the contribution from the scalar form factor $f_s(p)$. The predicted value of 1.5 fm^2 can be reproduced easily by assuming a core contribution (similar to that for ω exchange) and a finite range effect.

To estimate the mean square radius of the p-α potential at low energies we have to know the scalar radius of the α particle, which can be composed out of the nucleon density and the relative wave function of the four nucleons in the 1 s state: $\langle r^2_\alpha\rangle = \langle r^2_N\rangle + \langle r^2_{1s}\rangle$. Using $\langle r^2_\alpha\rangle$ and $\langle r^2_N\rangle$ from Ref. [12], we obtain $\langle r^2_{1s}\rangle \simeq 1.3$ fm^2 for the relative wave function of the four nucleons. If we use the same value also for the scalar part, we obtain a lower limit for the scalar radius of the α particle of about 3 fm^2. An upper limit is obtained by scaling the high energy α-particle radius by the ratio of scalar to vector radius of the nucleon, which would give $\langle r^2_\alpha\rangle_s \sim 4$ fm^2. A quite realistic estimate, $\langle r^2_\alpha\rangle_s \sim 3.5$ fm^2, is obtained by comparing the scalar potential to the nucleon σ term (discussed below). The form factor $f_s(p)$ adds a mean square radius of 0.8 fm^2. Still, an additional finite range of the scalar 2π-exchange interaction with $\gamma\sim 1.2$ fm is needed to obtain a potential mean square radius of 7 fm^2, consistent with the low-energy data. The results, with coupling strengths consistent with the potential depths in Table III, are given by the solid line in Fig. 7. They yield a good description of the deduced radii.

The above conclusions for the scalar potential can be checked by requiring that the scalar meson-exchange potential at beam momentum $p=0$ is constrained by the nucleon σ term [51] investigated in the timelike region. Approximating the scalar interaction of finite range γ by the σ term, this gives $v_s(\tilde{r}) = \sigma e^{-\tilde{r}^2/\gamma^2}$. Using $\sigma = 45$ MeV from Ref. [51], we get a volume integral of about 450 MeV fm^3 (as extracted at $E_p=0$ from the fit in Fig. 6) if a range $\gamma\sim 1.2$ fm is used. This is in agreement with the above results for $\langle r^2_\alpha\rangle_s = 3.5$ fm^2.

From the above analysis we can also extract the radius of the NN potential, which is given in Fig. 7 by the lower solid line. We obtain a similar behavior as for p-α scattering, but the increase of the radius at small energies is weaker. This is in excellent agreement with the extracted radius of the NN potential [44] given by the dotted line. Note that at smaller energies, where our results deviate from the dotted line, NN scattering shows no diffractive pattern, and the radius of the potential is not determined by the data.

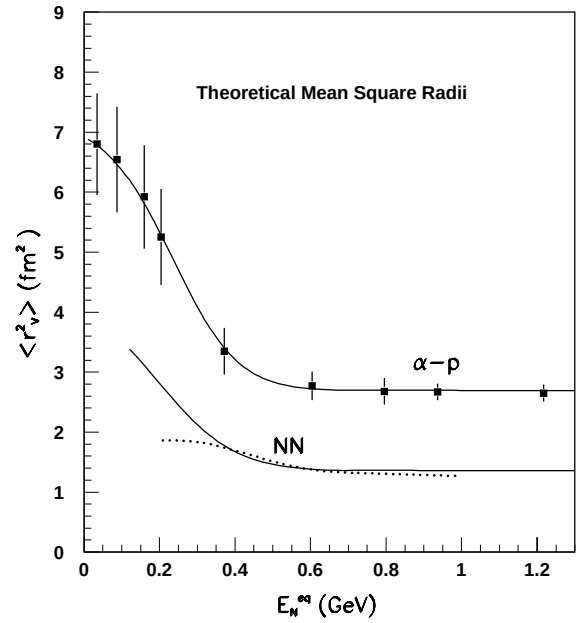

FIG. 7. Calculated mean square radius of the α-p potential (upper solid line) in comparison with the average α-p data in Fig. 3. Below are results for NN scattering, our radii given by the solid line in comparison with the NN potential of Ref. [44] (dotted line).

Finally, we want to make a comment about the core mean square radii, for which a value $\langle r^2 \rangle_{core} \sim 0.25$ fm^2 was obtained. According to the above discussion, this would correspond to a core form factor with a slope parameter $\kappa_{core} \sim 1.1$ (GeV/c)$^{-2}$. However, such a large effect is not seen in the energy dependence, suggesting, that κ_{core} must be much smaller ($< \kappa_\omega$). Indeed, also π exchange falls off up to 5–10 GeV, indicating $\kappa_{core} \leqslant 0.2$ (GeV/c)$^{-2}$. Therefore, to reproduce the experimental radii, ''effective'' masses for the exchanged mesons have to be introduced in Eq. (17), which are (for the vector mesons) reduced by about 20% with respect to the real masses.

C. Spin-orbit strengths

The energy dependence of the spin-orbit potential is quite different from the central potential, but also the uncertainties are much larger. In Fig. 8 the volume spin-orbit potential (with estimated uncertainties) is compared with a theoretical fit using the parameters in Table III. The surface potential has even larger uncertainties and is not further discussed. As for the central potential, the imaginary spin-orbit potential is well described assuming contributions from the repulsive force only.

The deduced vector coupling strenghts (for both volume and surface parts) are strongly enhanced relative to the other couplings; this is reflected in the large differences between Figs. 6 and 8. Similar to the differences in the central potential for p-α and NN discussed in Sec. IV A, this can be understood by different spin couplings: for the central p-α potential, only $\Delta J = 0$ and $\Delta I = 0$ contribute, whereas also $\Delta J = 1$ and $\Delta I = 1$ amplitudes contribute to the spin-orbit potential.

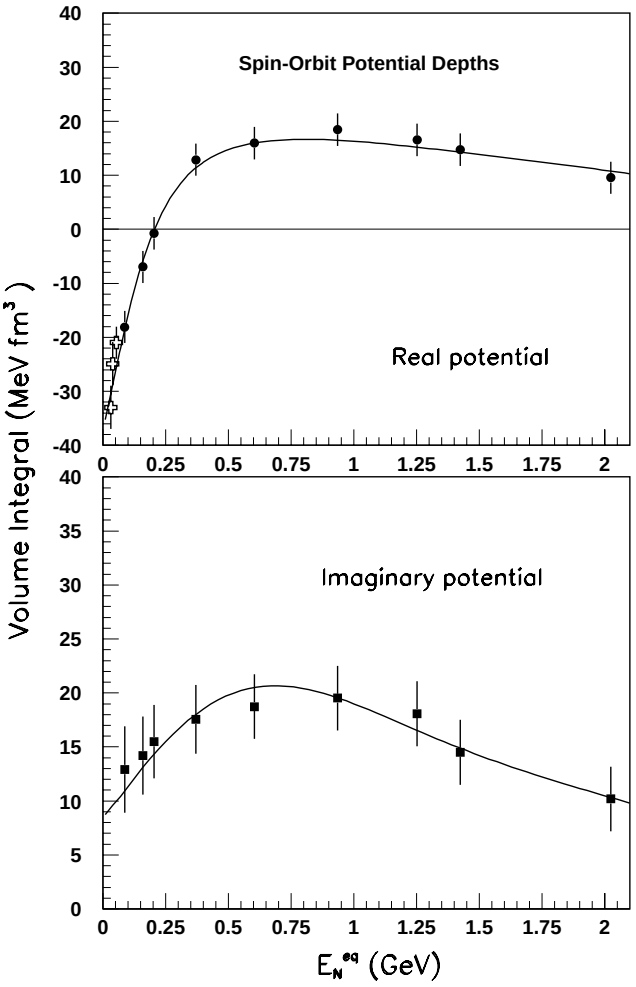

FIG. 8. Calculated depth of the volume spin-orbit potential with coupling strengths in Table III in comparison with the results in Table I, the results of Ref. [23] are given by the open points.

In contrast to the central potential, the spin-orbit potential falls off towards large energies, indicating that a soft Pomeron contribution is small. Studies of the Pomeron have shown that its spin-flip amplitude should be very small [53]. This is consistent with our observation, which suggests that this property of the Pomeron is not changed by going into the soft scattering regime.

Finally, it is interesting to note that in the relativistic study [8] an increase of the Lorentz scalar potential towards the highest energies was observed. From Figs. 5–8, we see that at these energies scalar meson exchange has already fallen off completely, but such a behavior is observed in our analysis for the soft Pomeron contribution. This shows a consistency of our analysis with that of Ref. [8].

D. NN amplitudes

Most direct information on the structure of the NN force is contained in the NN phase shift amplitudes, which are available [54] for p-p up to 3 GeV and for p-n up to 1.2 GeV. These can be used for a detailed test of our meson exchange and soft Pomeron potentials. We made calculations of the s-wave amplitudes (see Fig. 9), which show the stron-

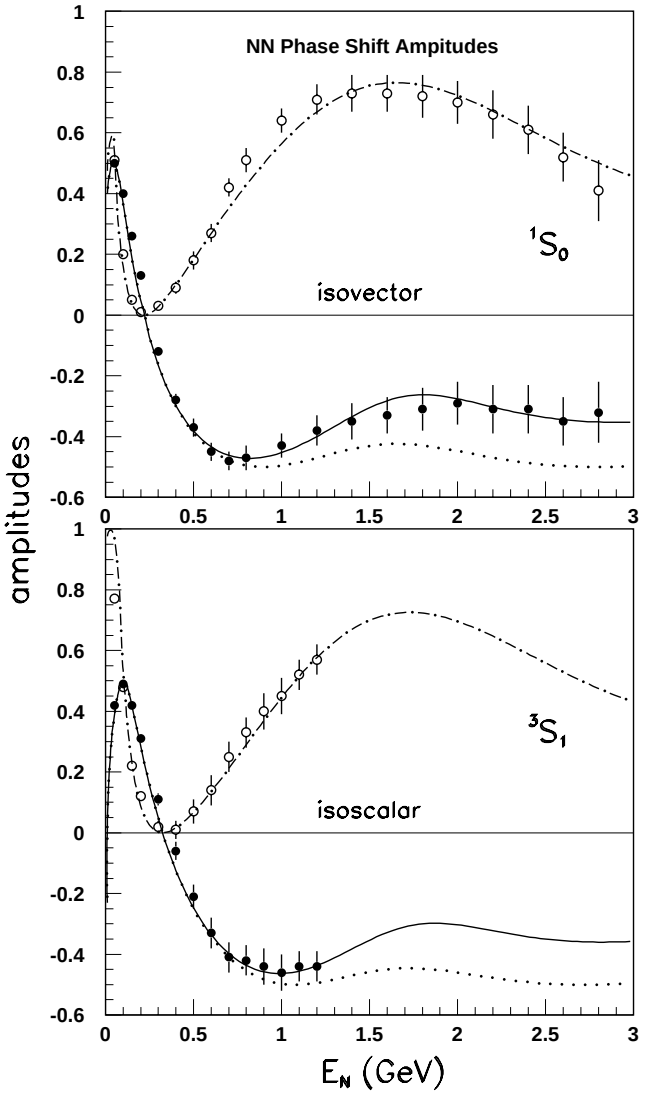

FIG. 9. Average nucleon-nucleon s-wave amplitudes (real given by solid points, imaginary by open points) from Arndt *et al.* [54] in comparison with our calculations. The dot-dashed lines represent a fit of the imaginary amplitudes, the dotted lines show the real t-matrix amplitudes (elastic only), whereas the solid lines indicate the real amplitudes including a small inelasticity linear with energy.

gest energy dependence. In the imaginary amplitudes all three large exchange components needed for the description of p-α scattering are observed directly: 2π exchange responsible for the strong rise at small energies, a large bump due to ω exchange centered at about 1.6 GeV, and the increase towards the highest energies due to soft Pomeron exchange. Different from p-α scattering, pseudoscalar π and η exchange can also contribute to NN scattering, and has been included in our calculations.

To calculate the NN phase shift amplitudes, a partial wave description of the NN scattering amplitude, $f(\theta,E) = (1/k)\Sigma_l(2l+1)\,[a_l^{re}(E)+ia_l^{im}(E)]P_l(\cos\theta)$, is needed. Using the optical theorem the imaginary amplitudes can be expressed by $a_l^{im}(E)=[(1/V_0)\Sigma_x V^x(E)|\overline{a}_{l,\gamma_x}(E)|]^2$, where x denotes the different exchange contributions discussed above with their potentials $V^x(E)$, and V_0 the potential strength at zero energy. Here $|\overline{a}_{l,\gamma_x}(E)|$ are normalized NN partial wave amplitudes of the differential cross section, calculated by using double-folding optical potentials as discussed in Sec. II. Calculations with different values of γ, long range for π and 2π exchange and short range for vector meson and soft Pomeron exchange, were performed, from which the partial wave amplitudes $\overline{a}^{re,im}_{l,\gamma_x}(E)$ were generated in small energy steps ranging from 0 to 3 GeV. To get a continuous energy dependence, these amplitudes were fitted by double-exponential forms. All partial wave amplitudes have been normalized, $\Sigma_l[\overline{a}^{re}_{l,\gamma_x}(E)^2+\overline{a}^{im}_{l,\gamma_x}(E)^2]=1$, at $E=1$ GeV. From these we obtain $|\overline{a}_{l,\gamma_x}(E)|=[\overline{a}^{re}_{l,\gamma_x}(E)^2 + \overline{a}\,a^{im}_{l,\gamma_x}(E)^2]^{1/2}$.

Using coupling constants given in Table III, the imaginary amplitudes are quite well described. For π exchange, only a small effective coupling $\overline{g}^2_\pi$ is needed to reproduce the position of the minimum in the imaginary amplitudes. For the other coupling a reasonable agreement is found with the bare couplings used by Machleidt *et al.* [16,47].

In t-matrix theory the real scattering amplitude $a_l^{re}(E)$ is related to the imaginary amplitude by $a_l^{re}(E) = \sqrt{a_l^{im}(E)-a_l^{im}(E)^2-\mathrm{in}a_l^{im}(E)}$, where $\mathrm{in}a_l^{im}(E)$ is the inelastic part of $a_l^{im}(E)$. First calculations have been done assuming $\mathrm{in}a_l^{im}(E)=0$, the results are given by the dotted lines in Fig. 9. At lower energies an excellent agreement with the experimental amplitudes [54] is found, which shows clearly the t-matrix character of the effective interaction. At higher energies deviations are observed due to an increase of inelasticity. If we assume $\mathrm{in}a_l^{im}(E)=0.1a_l^{im}(E)(E-E_{thr})$, where E_{thr} is the inelastic threshold, we obtain a quantitative description of the real amplitudes (solid lines in Fig. 9). The decrease of the real amplitude at increasing energy is quite the same as for the real soft Pomeron-exchange potential (16) shown in Fig. 5 and indicates the consistency of our description. Finally it should be mentioned that in our folding approach (Sec. II) the complete momentum dependence of the scattering amplitude is taken into account. This is different from the usual meson-exchange approach [16,47], in which the t dependence is assumed of much simpler form.

V. INELASTIC α-p SCATTERING EXCITING N^* RESONANCES

Finally, we come to the discussion of inelastic α-p scattering. We restrict our calculations to the excitation of N^* resonances in the proton by the α particle, $\alpha+p\rightarrow\alpha' N^*$; excitation of the α particle, which has a different kinematics (see Refs. [11,55]), is only discussed in comparison with the experimental data. The differential cross section for initial energy E is given as a function of mass m in distorted wave Born approximation (DWBA) [14] by

$$\frac{d\sigma}{d\Omega}(E,m)=(2J_i+1)(2L+1)(4\pi)^2\left|\int \Psi_f^\dagger(E-m,\vec{k}',\vec{r}) \times U_{tr}(E,\vec{r})\Psi_i(E,\vec{k},\vec{r})d\vec{r}\right|^2, \quad (18)$$

where Ψ_i and Ψ_f are solutions of the Schrödinger equation for the initial and final state with the optical potentials (7). In the DWBA calculations relativistic kinematics is used. The inelastic transition potential $V_{tr}(m,\vec{r})$ is given by

$$U_{tr}(E,\vec{r}) = \int\int \rho^{tr}_{N*}(\vec{r}_1)\rho_2(\vec{r}_2)u(E,\vec{r}+\vec{r}_1-\vec{r}_2)d\vec{r}_1 d\vec{r}_2, \tag{19}$$

where $\rho^{tr}_{N*}(\vec{r}_1)$ represents an extended $p\rightarrow N^*$ transition density, $\rho_2(\vec{r}_2)$ the α-particle ground state density, and $u(\vec{r}+\vec{r}_1-\vec{r}_2)$ the same effective interaction as in Eq. (6), as determined from elastic scattering at the energy of the initial α-p system. The study of broad N^* resonances requires DWBA calculations at many energies in the exit channel; the theoretical potentials discussed in Sec. IV yield a smooth energy dependence and could be inserted directly in our calculations.

The maximum excitation strength for scalar interaction with angular momentum L is given by an energy weighted sum rule limit (see Refs. [12,56]). Using transition operators of the form $[1/(2L+1)^{1/2}]r^{(L+2)}Y_L$ for $L=0$, 1 and $[1/(2L+1)^{1/2}]\,r^L Y_L$ for higher L, the energy weighted sum rule [56] for $L=0$ is given by

$$S(L=0) = \sum_i E_i |\langle r^2 Y_0\rangle|^2 = \frac{9(\hbar c)^2}{2\pi m}\langle r^2_{\rm g.s.}\rangle. \tag{20}$$

For $L=1$ excitation, the c.m. recoil of the nucleon has to be taken into account; this yields

$$S(L=1) = \frac{1}{3}\sum_i E_i |\langle r^3 Y_1\rangle|^2 = \frac{33(\hbar c)^2}{8\pi m}\langle r^4_{\rm g.s.}\rangle\left[1-\frac{25\langle r^2_{\rm g.s.}\rangle^2}{33\langle r^4_{\rm g.s.}\rangle}\right]. \tag{21}$$

For excitation of higher L values, we obtain

$$S(L) = \frac{1}{(2L+1)}\sum_i E_i |\langle r^L Y_L\rangle|^2 = \frac{L(2L+1)9(\hbar c)^2}{8\pi m}\langle r^{2L-2}_{\rm g.s.}\rangle. \tag{22}$$

A. Transition densities

For scalar excitation of the lowest natural parity N^* resonances [with quantum numbers $J=L+\frac{1}{2}$ and $\pi=(-1)^L$], the transition densities $\rho^{tr}_{N*}(\vec{r})$ may be described in a fluid-dynamical approach (similar to the Skyrmion model; see, e.g., Ref. [57]) by a distortion of the ground state density [12], but also the overlap of radial wave functions $\rho^{tr}_{N*}(\vec{r}) = u_f(\vec{r})\cdot u_i(\vec{r})$ from quark models may be used. If the particle number $\int \rho_i(r)d\tau$ is not changed between the initial and the final state, this requires for radial ($L=0$) excitations $\int \rho^{tr}_{N*}(r)r^2 dr = 0$. Assuming a monopole vibration of the nucleon similar to that used in Ref. [12] (with a g.s. density of exponential form), a transition density is obtained as given by the solid line in Fig. 10. A corresponding $1s\rightarrow 2s$ constituent quark transition gives $\rho^{tr}_{N*}(r)$, as shown by the dot-dashed line.

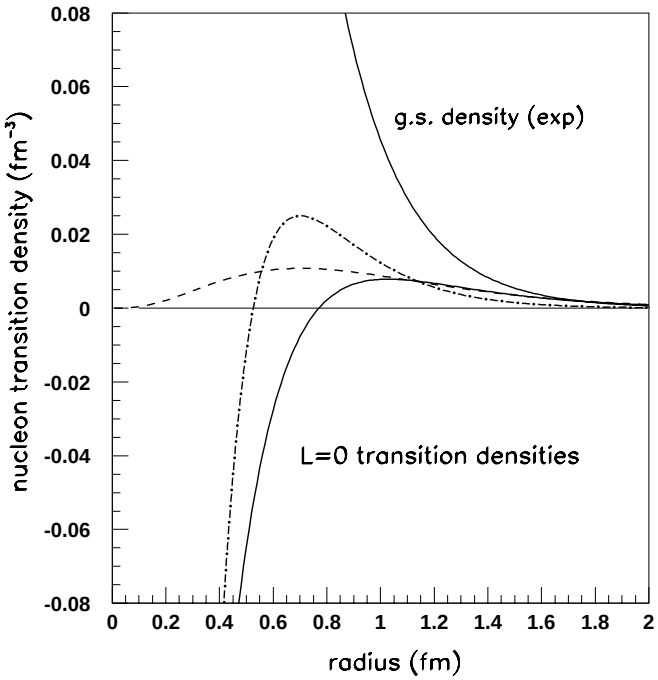

FIG. 10. $L=0$ transition densities for monopole vibration of the nucleon (solid line), approximate form of $1s\rightarrow 2s$ quark excitation (dot-dashed line), and $N\rightarrow\sigma N$ transition (dashed line). The g.s. density is given by the upper solid line.

There are large differences between these transition densities. As α-p scattering is sensitive to the surface region [the differential cross section (18) scales roughly with $\langle r^2_{tr}\rangle$], this gives much larger cross sections for the case of a monopole density vibration (see below). On the other hand, in α-p we are insensitive to the inside part of the transition density, which is also of large interest. In relativistic models the node in the transition density can move towards $r=0$, if the transition proceeds entirely by $(q\bar{q})^n$ production. In this respect a $N\rightarrow\sigma N$ transition is of interest (although the width of the σ or 2π correlation is much larger than the width of our P_{11} resonance), and an estimate of the corresponding transition density is given by the dashed line in Fig. 10. Information on the small radius behavior of the transition density can be obtained from a detailed comparison of α-p and electron scattering. We expect much larger relative (e,e') cross sections for a $N\rightarrow\sigma N$ transition (dashed line) than for a vibration of the nucleon density (solid line). Preliminary results from $(e,e'x)$ experiments at JLab [58], however, show very little evidence for excitation of the scalar part of the $P_{11}(1440)$ resonance, which is very strong in α-p. This is in favor of a transition density with a nodal structure similar to the solid line, which gives strong cancellations in (e,e'). Interestingly, for sound modes of higher L, the node in the

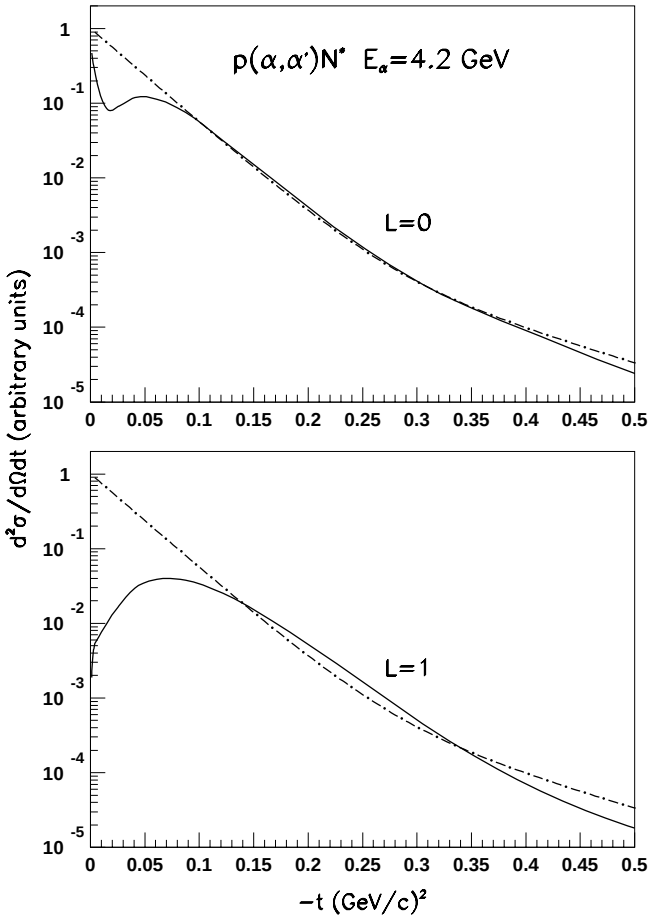

FIG. 11. t-Dependence of the DWBA cross sections at 0° for $L=0$ and 1 transitions (solid lines) in comparison with the empirical α-p form factor [55] fitted to the experimental data (dot-dashed lines).

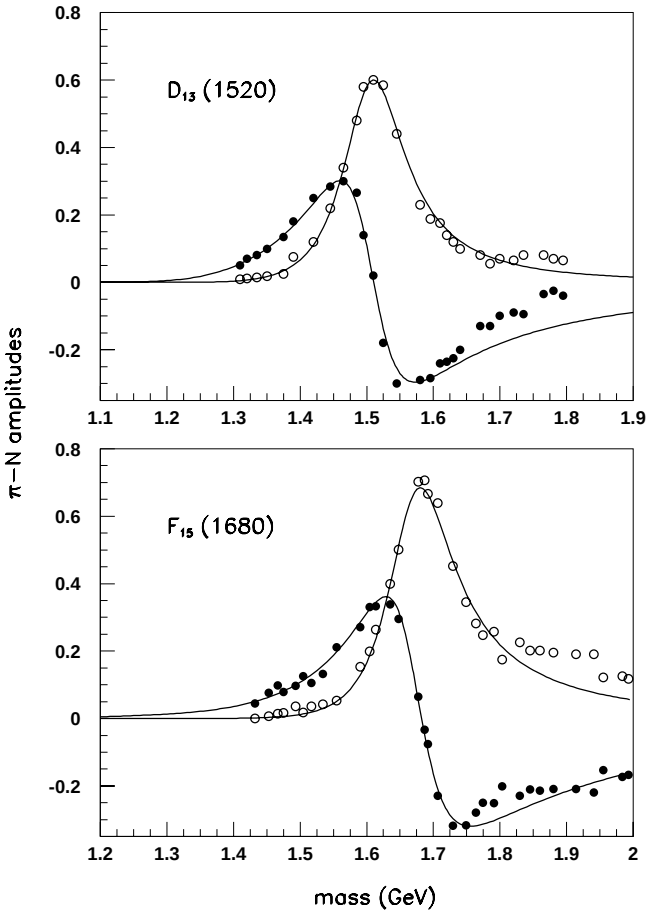

FIG. 12. π-N amplitudes for D_{13} and F_{15} (real and imaginary parts given by solid and open points, respectively) from Ref. [59] in comparison with modified Breit-Wigner shapes with the parameters in Table IV.

transition density moves to larger radii and gives also cancellations in α-p scattering.

B. Comparison with experimental data and results

In the analysis of the experimental spectra at $E_\alpha = 4.2$ GeV [11], the t dependence of the differential cross section $[t=(1/c^2)(E_\alpha - E_{\alpha'})^2 - (\vec{p}_\alpha - \vec{p}_{\alpha'})^2]$ has been well described (see Ref. [55]) by an empirical α-p form factor $F(|t|)^2 = \exp(-k_1|t|) + \exp[-k_2|t| - (k_1-k_2)t_o]$ with the constants k_1 and k_2 of 29 and 10 $(\mathrm{GeV}/c)^{-2}$ and $t_0 = 0.25$–0.27 $(\mathrm{GeV}/c)^2$. This exponential form is compared in Fig. 11 with the t dependence of the DWBA cross section at 0° scattering angle. For $L=0$ excitation the DWBA results show a minimum at small momentum transfer, which reflects the diffractive structure seen in elastic scattering. This, however, is not important for the observed shape of the $P_{11}(1440)$ resonance, which is excited with larger momentum transfers. Therefore it is quite impressive that the falloff of the empirical form factor over three orders of magnitude is well described by the DWBA calculation. For higher L transfers the DWBA calculations show some deviations from this empirical form.

Scalar excitation of the resonances $P_{11}(1440)$, $D_{13}(1520)$, and $F_{15}(1680)$ can contribute to the α-p spectrum of Ref. [11]. For the shapes of these resonances modified Breit-Wigner forms [55] were used, which yield good fits of the π-N amplitudes. For the scalar part of the $P_{11}(1440)$ (Saturne resonance), the details are discussed in Ref. [55], fits of the π-N amplitudes from Ref. [59] for $D_{13}(1520)$ and $F_{15}(1680)$ are given in Fig. 12, using the same mass dependent width (see Ref. [55]) as applied for the $P_{11}(1440)$ resonance. The resulting resonance parameters are given in Table IV. We found, that a quantitative fit of π-N in the lower resonance mass region is essential to determine the shape of the resonance in α-p scattering.

Differential cross sections for N^* excitations with $L=0$ and 1 at 0° are given in Fig. 13 as a function of N^* mass. An upper cross section limit is obtained by using fluid-dynamical transition densities (for $L=0$ given by the solid line in Fig. 10), which are constrained by sum rules (20) and (21) (using for E the centroid energy of the corresponding resonance). In Fig. 13 the resonance shapes for $P_{11}(1440)$ and $D_{13}(1520)$ are also shown (dot-dashed lines), as well as the resulting shapes for α-p (histograms). The differential cross section at 0° for $L=0$ excitation is about 100 mb/sr at

TABLE IV. Modified Breit-Wigner resonance parameters (see the definition in Ref. [55]). For the $P_{11}(1440)$ the parameters of the scalar part (Saturne resonance) are given. The sum rule fractions are determined by a fit of the α-p spectrum in Fig. 14.

Parameter	$P_{11}(1440)$	$D_{13}(1520)$	$F_{15}(1680)$
Mass (MeV)	1390	1510	1680
Width (MeV)	190	115	125
$B_{\pi\text{-}N}$ (Γ^{el}/Γ)	0.30	0.61	0.71
Background	0.0	0.02	0.08
C_{thres}	8.0	4.8	4.0
C_{cut}	0.1	2.0	1.5
Extracted sum rule	$L=0$	$L=1$	$L=2$
Fractions in α-p	75–100 %	50–80 %	80–100 %

the centroid of the $P_{11}(1440)$, this is about the size of the experimental cross section for this resonance [11]. Our results are rather close to the less detailed calculations in Ref. [12] and confirm the previous conclusions. Here it should be noted that the use of a constituent quark model transition density (dot-dashed line in Fig. 10) underpredicts the experimental cross section by more than a factor of 4.

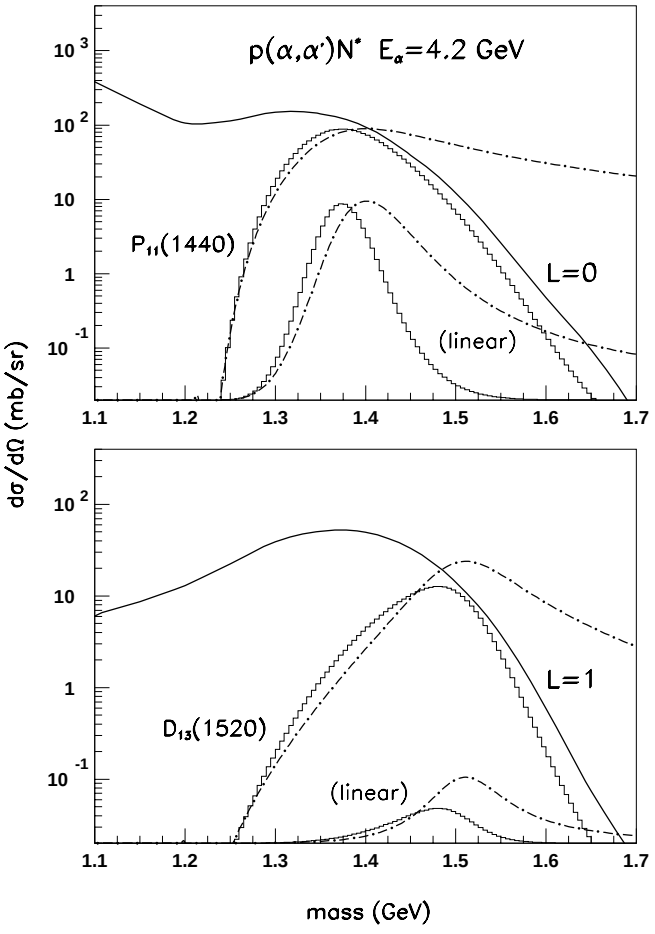

FIG. 13. Differential cross sections at 0° in the lab system for $L=0$ and 1 excitation as a function of mass (solid lines). The shapes of the lowest N^* resonances from π-N (see Ref. [55] and Fig. 12) are given by the dot-dashed lines, and the resulting resonance shapes in α-p by the histograms. Below, the corresponding shapes are given in linear scale with arbitrary normalization.

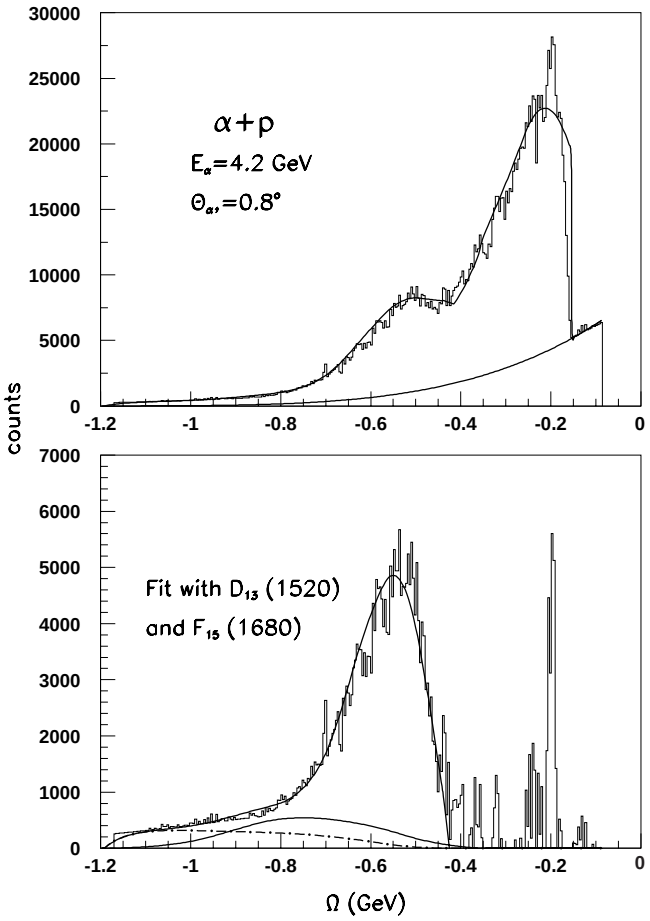

FIG. 14. Calculated missing energy spectra of inelastic α-p scattering in comparison with the data from Ref. [11]. In addition to projectile excitation and the $P_{11}(1440)$ (as in Ref. [55]), contributions from the $D_{13}(1520)$ and $F_{15}(1680)$ resonances (lower solid and dashed line, respectively) are included.

For $L=1$ excitation the differential cross section has already fallen off strongly at the mass centroid of the $D_{13}(1520)$. Therefore, this resonance is not strongly excited in α-p at this incident energy, but may contribute to the ''background'' under the Roper resonance. For even higher N^* resonances [e.g., the $F_{15}(1680)$], the available c.m. energy is not sufficient to excite the full resonance, but a contribution from the low-mass tail is still possible.

To see whether excitation strength of higher N^* resonances can be accomodated in the observed α-p spectra, we made calculations of the inclusive α-p spectrum similar to those in Ref. [55], including also the interference between N^* excitations in the target and Δ projectile excitation. We assumed an instrumental background similar to that in Ref. [11], which arises only from the tail of elastic scattering caused by multiple scattering within the collimator (see Fig. 14). The ''background'' at higher energy transfers should be entirely due to excitation of N^* resonances. Using the resonance shapes given by the histograms in Fig. 13, the corresponding resonance shapes in the Ω spectrum were calcu-

lated by the Monte Carlo method and fitted by spline functions. We found, that the $D_{13}(1520)$ can be accomodated below the $P_{11}(1440)$ with a $L=1$ sum rule fraction of up to about 80%. We see, however, that this resonance (lower solid line in Fig. 14) has fallen off almost entirely at an energy transfer of 1 GeV, where the experimental yield is still rather high. By including the $F_{15}(1680)$ with a sum rule strength close to 100%, a quite reasonable description of the inclusive spectrum is obtained. The contribution of this resonance is given by the dot-dashed line in Fig. 14, a fit including all resonances by the upper solid lines (with the sum rule fractions in Table IV). More detailed information on the excitation of higher N^* resonances can be obtained only from exclusive experiments. Indeed, preliminary results from the exclusive α-p experiment [60] support our interpretation, yielding evidence for excitation of higher N^* resonances, in particular of the $D_{13}(1520)$.

The spectroscopic results for the different resonances in Table IV deserve some attention. The $D_{13}(1520)$ is observed in α-p, but is also excited in photoinduced reactions [61], which corresponds to isovector excitation. The fact that this resonance is seen in both reactions indicates excitation of mixed isospin. Consequently, one should not see the full energy weighted sum rule strength in α-p. This is in agreement with the result of our fit. On the other hand, the fact that large scalar sum rule fractions are obtained for all three N^* excitations in Table IV indicate rather pure scalar (non-spin-isospin-flip) excitations, supporting a picture of these resonances in terms of sound modes (breathing mode for $L=0$, see Ref. [56]). As discussed above, the cross sections cannot be described in the constituent quark model; further, such pure scalar modes are not expected in a quark model picture in which scalar and spin-isospin amplitudes should be mixed. For the Roper resonance this would indicate a mixture of scalar and $M1$ excitation, the latter has been found in $p(\gamma,2\pi^0)$ for the second component of the $P_{11}(1440)$ resonance [55], which has a structure different from the scalar excitation studied here.

C. Estimates for p-α scattering at higher c.m. energies

From the previous discussion studies of N^* excitations in α-p at higher c.m. energies appear very interesting. Experimentally, such investigations are possible in reverse kinematics using a proton beam up to 2.5 GeV and a liquid ^{4}He target. We have calculated cross sections of p-α scattering at $E_p=2.2$ GeV, which are compared with the cross sections of α-p scattering at $E_\alpha=4.2$ GeV in Fig. 15. Invariant cross sections for $L=0$ and 1 excitation in forward direction for $E_\alpha=4.2$ GeV are given by the solid lines, and those of p-α scattering at $E_p=2.2$ GeV by the dashed lines. We observe generally a large increase of the cross sections in the region of higher masses. In addition, Fig. 15 shows the effect on the excitation of the $P_{11}(1440)$ and $D_{13}(1520)$ resonances (in linear scale): the dot-dashed lines indicate the resonance shapes deduced from π-N, whereas the histograms give the corresponding shapes in α-p at the lower and higher c.m. energies. For the $P_{11}(1440)$ excitation, an increase of the differential cross section of a factor 6 at the higher c.m. energy is obtained, and for the $D_{13}(1520)$ resonance an increase of about 24 is obtained. This will allow us a more detailed study of N^* excitations, provided that at the higher energy fully exclusive data over a wide angle range can be measured, from which a multipole decomposition is possible.

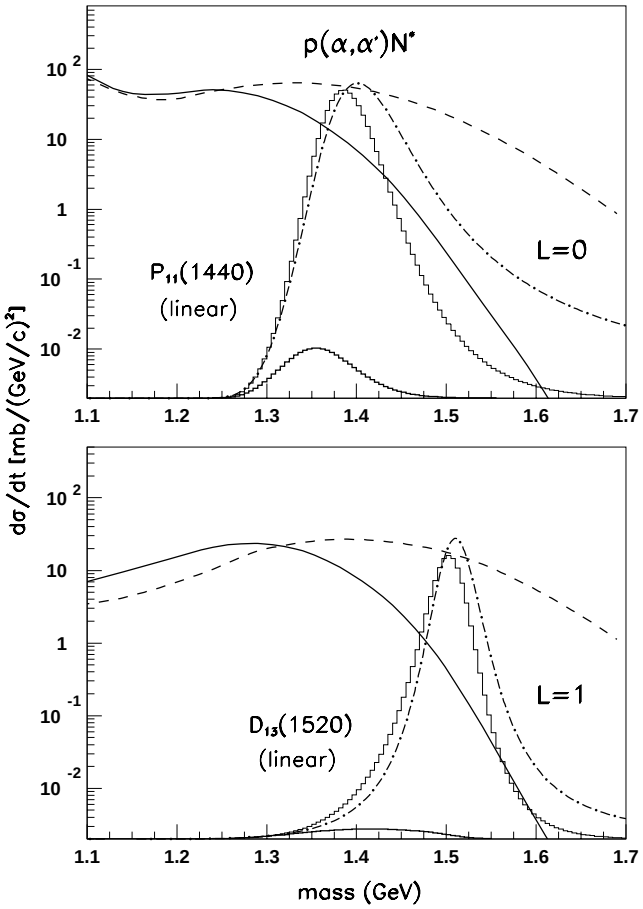

FIG. 15. Invariant cross sections at minimum momentum transfer for $L=0$ and 1 excitation at $E_\alpha=4.2$ GeV (solid lines) and at $E_p=2.2$ GeV (dashed lines) as a function of mass. The resonance shapes (dot-dashed lines) are the same as in Fig. 13, the histograms with small and large heights show the shapes in α-p at the lower and higher c.m. energy, respectively. All resonance shapes are given in linear scale with the relative strengths normalized.

VI. CONCLUSION

The present investigation has shown that a reliable description of forward elastic α-scattering data from low energies up to several GeV has been obtained in the folding model, from which new information on the energy dependence of the optical potential could be extracted, in particular on its radius. By the investigation of α-α and α-^{12}C, it was checked that the folding model approach is valid for the systems in question.

The deduced potentials could be described by scalar and vector meson exchange, but also a soft multigluon-exchange contribution is needed, which becomes increasingly important at higher energies. In this description the introduction of decay form factors for the exchanged ''mesons'' (extension

of the one-meson exchange picture to more-meson exchange) was essential to describe the low- and high-energy behavior and the large change in the potential radii. With the introduction of a soft Pomeron contribution and meson-exchange form factors, we see the connection to the high-energy description of NN scattering in terms of Regge trajectories: the meson-exchange form factor falloffs can be identified with negative slope Regge trajectories and the soft Pomeron exchange to a very small positive Regge slope. Therefore, the present picture of the effective potential is valid from very small energies up to the multi-GeV region.

For inelastic scattering, the present study has shown that the differential cross sections are quite reliably described by DWBA calculations using effective interactions deduced from elastic scattering. From the data of α-p scattering, important spectroscopic information on N^* resonances is extracted, which is in severe conflict with the constituent quark model. It appears that a new degree of freedom comes into play (most likely due to gluons), which gives rise to strong excitation of sound modes.

The cross sections increase strongly with c.m. energy, this makes a study of N^* resonances in p-α scattering with a proton energy of the order of about 2.5 GeV very interesting. The special character and the high selectivity of α scattering is well suited to complement studies of baryon resonances with electromagnetic probes.

ACKNOWLEDGMENTS

Fruitful discussion with M. Rekalo, R. Machleidt, T. Barnes, and N. N. Nikolaev is acknowledged. In particular, we thank P. Zupranski for his help in solving detailed problems and S. Krewald for many enlightening discussions and a careful reading of the paper.

[1] L. Ray, G.W. Hoffmann, and W. R. Coker, Phys. Rep. **212**, 223 (1992), and references therein.
[2] R.J. Glauber and G. Matthiae, Nucl. Phys. **B21**, 137 (1970); S.K. Young and C.W. Wong, Phys. Rev. C **15**, 2146 (1977).
[3] J.P. Auger, J. Gillespie, and R.J. Lombard, Nucl. Phys. **A262**, 372 (1976); R. Dymarz and A. Malecki, Phys. Lett. **66B**, 413 (1977).
[4] H.F. Arellano, F.A. Brieva, and W.G. Love, Phys. Rev. C **41**, 2188 (1990).
[5] B.C. Clark, S. Hama, R.L. Mercer, L. Ray, and B.D. Serot, Phys. Rev. Lett. **50**, 1640 (1983).
[6] S.W. Leung and H.S. Sherif, Can. J. Phys. **56**, 1116 (1978), and references therein.
[7] G.D. Alkhazow *et al.*, Sov. J. Nucl. Phys. **41**, 357 (1985).
[8] L.G. Arnold, B.C. Clark, and R.L. Mercer, Phys. Rev. C **19**, 917 (1979), and references therein.
[9] J.J. Kelly and S.J. Wallace, Phys. Rev. C **49**, 1315 (1994); L. Kurth *et al., ibid.* **49**, 2086 (1994).
[10] L. Ray, Phys. Rev. C **49**, 2109 (1994).
[11] H.P. Morsch *et al.*, Phys. Rev. Lett. **69**, 1336 (1992).
[12] H.P. Morsch, W. Spang, and P. Decowski, Z. Phys. A **348**, 45 (1994).
[13] S. Hirenzaki, P.F. de Cordoba, and E. Oset, Phys. Rev. C **53**, 277 (1996).
[14] G.R. Satchler, Nucl. Phys. **A55**, 1 (1965).
[15] G.W. Greenlees, G.J. Pyle, and Y.C. Tang, Phys. Rev. **171**, 1115 (1968); see also C.J. Batty, E. Friedman, H.J. Gils, and H. Rebel, Adv. Nucl. Phys. **19**, 1 (1989).
[16] R. Machleidt, Adv. Nucl. Phys. **19**, 189 (1989), and references therein.
[17] M. Oka and K. Yazaki, Phys. Lett. **90B**, 41 (1980); T. Barnes, S. Capstick, M.D. Kovarik, and E.S. Swanson, Phys. Rev. C **48**, 539 (1993), and references therein.
[18] A. Donnachie and P.V. Landshoff, Nucl. Phys. **B231**, 189 (1984); **B311**, 509 (1989).
[19] J. Hüfner and B. Povh, Phys. Rev. D **46**, 990 (1992), and references therein.
[20] W.G. Love and M.A. Franey, Phys. Rev. C **24**, 1073 (1981).
[21] K.M. Watson, Phys. Rev. **89**, 575 (1953); **105**, 1388 (1957).
[22] B. Povh and J. Hüfner, Phys. Lett. B **245**, 653 (1990).
[23] G.E. Thompson, M.B. Epstein, and T. Sawada, Nucl. Phys. **A142**, 571 (1970).
[24] L.G. Votta *et al.*, Phys. Rev. C **10**, 520 (1974).
[25] V. Comparat *et al.*, Phys. Rev. C **12**, 251 (1975); for analyzing powers, A.M. Cormack *et al.*, Phys. Rev. **115**, 599 (1959).
[26] J. Berger *et al.*, Phys. Rev. Lett. **37**, 1195 (1976).
[27] E. Aslanides *et al.*, Phys. Lett. **68B**, 221 (1977).
[28] R. Klem *et al.*, Phys. Lett. **70B**, 155 (1977).
[29] R. Klem *et al.*, Phys. Rev. Lett. **37**, 1272 (1977).
[30] J. Fong *et al.*, Phys. Lett. **78B**, 205 (1978).
[31] G.A. Moss *et al.*, Phys. Rev. C **21**, 1932 (1980).
[32] L. Satta *et al.*, Phys. Lett. **139B**, 263 (1984).
[33] G.N. Velichko *et al.*, Sov. J. Nucl. Phys. **42**, 837 (1985).
[34] H.P. Morsch *et al.*, Z. Phys. A **350**, 167 (1994); **353**, 349 (1995).
[35] B. Brinkmöller *et al.*, Phys. Rev. C **42**, 550 (1990)
[36] J. Berger *et al.*, Nucl. Phys. **A338**, 421 (1980).
[37] R. Dymarz and A. Malecki, Phys. Lett. **83B**, 15 (1979).
[38] J.C. Fong *et al.*, Nucl. Phys. **A262**, 365 (1976).
[39] W.S. Chien and R.E. Brown, Phys. Rev. C **10**, 1767 (1974).
[40] A. Nadasen *et al.*, Phys. Rev. C **18**, 2792 (1978).
[41] K.A.G. Rao *et al.*, Phys. Rev. C **62**, 014607 (2000).
[42] A. Chaumeaux *et al.*, Nucl. Phys. **A267**, 413 (1976).
[43] I. Reichstein and Y.C. Tang, Nucl. Phys. **A139**, 144 (1969), and references therein.
[44] M.A. Franey and W.G. Love, Phys. Rev. C **31**, 488 (1985).
[45] R.A. Arndt *et al.*, Phys. Rev. D **28**, 97 (1983).
[46] M. Kleinmann, R. Fritz, H. Müther, and A. Ramos, Nucl. Phys. **A579**, 85 (1994).
[47] R. Machleidt, K. Holinde, and Ch. Elster, Phys. Rep. **149**, 1 (1987).
[48] D. Plümper, J. Flender, and M.F. Gari, Phys. Rev. C **49**, 2370 (1994).
[49] G.G. Simon, F. Borkowski, C. Schmitt, and V.H. Walther, Z. Naturforsch. A **35A**, 1 (1980).
[50] I. Sick, J.S. McCarthy, and R.R. Whitney, Phys. Lett. **64B**, 33 (1976).

[51] J. Gasser, H. Leutwyler, and M.E. Sainio, Phys. Lett. B **253**, 260 (1991).
[52] B.C. Pearce, K. Holinde, and J. Speth, Nucl. Phys. **A541**, 663 (1992).
[53] B.G. Zakharov, Sov. J. Nucl. Phys. **49**, 860 (1989); B.Z. Kopeliovich and B.G. Zakharov, Phys. Lett. B **226**, 156 (1989); see also N.H. Buttimore *et al.*, Phys. Rev. D **59**, 114010 (1999), and references therein.
[54] R.A. Arndt, I.I. Strakovsky, and R.L. Workman, Phys. Rev. C **62**, 034005 (2000).
[55] H.P. Morsch and P. Zupranski, Phys. Rev. C **61**, 024002 (1999).
[56] H.P. Morsch, Z. Phys. A **350**, 61 (1994).
[57] B. Schwesinger, Nucl. Phys. **A537**, 253 (1992), and references therein.
[58] V. Mokeev *et al.*, in *Proceedings of the N*2002 workshop*, edited by S. Dytman and E. Swanson (to be published); V. Burkert (private communication).
[59] R.A. Arndt, I.I. Strakowsky, R.L. Workman, and M.M. Pavan, Phys. Rev. C **52**, 2120 (1995), and references therein.
[60] G.D. Alkhazov *et al.*, in *Proceedings of the COSY workshop on "Baryon Excitations," Jülich, 2000*, edited by T. Barnes and H.P. Morsch [Schr. FZ-Jülich 6, **53** (2000)]; (to be published).
[61] M. MacCormick *et al.*, Phys. Rev. C **53**, 41 (1996); A. Braghieri, *et al.*, Phys. Lett. B **363**, 46 (1995); M. Wolf *et al.*, Eur. Phys. J. A **9**, 5 (2000), and references therein.